Annu. Rev. Mater. Sci. 1995. 25: 129–60

MAGNETISM AND GIANT MAGNETO-TRANSPORT PROPERTIES IN GRANULAR SOLIDS

C. L. Chien

Department of Physics and Astronomy, The Johns Hopkins University, Baltimore, Maryland 21218

KEY WORDS: magnetic properties, giant magnetoresistance, Hall resistivity, magneto-thermal conductivity

ABSTRACT

Magnetic granular solids consist of nanometer-sized magnetic particles uniformly dispersed and embedded in an immiscible insulating or metallic medium. They display a rich variety of magnetic properties and giant magneto-transport properties due to their unique nanostructure, which can be usefully described by the metal volume fraction and the metal particle diameter of granular solids. Fabrications and characterizations of granular solids, their enhanced magnetic properties, percolation behavior, single-domain characteristics, superparamagnetic relaxation, and superparamagnetism are reviewed. Giant magneto-transport properties, recently observed in granular solids, including giant magnetoresistance, extraordinary Hall resistivity, magneto-thermal conductivity, and Wiedemann-Franz law are discussed.

INTRODUCTION

Granular metal solids, consisting of ultrafine metallic particles uniformly dispersed and embedded in an immiscible medium, constitute a special class of artificially structured materials (ASM) with low-dimensional entities (1). Multilayers (2) and arrays of nanowires (3) are ASM with quasi two-dimensional and one-dimensional entities respectively; granular solids

0084–6600/95/0801–0129$05.00

have quasi zero-dimensional entities. The novel properties of granular solids arise from the unique nanostructure with which their properties can be altered and tailored. Granular metal solids, pioneered by Abeles et al (4, 5), have recently attracted considerable renewed interest. This is due in part to the current interest in nanophase materials (6–8), and to the unusual physical properties that have been uncovered in granular metal solids. The word granular has also appeared in other contexts, most notably in the studies of fluid flowing through rocks and experiments on sand piles at the threshold of instability. The key difference is the size of the granules, which are of the order of 10 cm in the case of rocks and 100 μm in sand grains. In the present context, granules are referred to as ultrafine solid particles, only a few nms in size, consisting of 10^3–10^6 atoms. Solids of such small sizes are between those of clusters and bulk solids. This is also the size range that is unattainable by usual powder metallurgical and chemical methods. Another important feature of granular solids is that these ultrafine particles are not free standing but are embedded in an immiscible medium. Free-standing ultrafine metallic particles are notoriously susceptible to environmental degradation (e.g. oxidation) and have a strong tendency to conglomerate into larger entities. Both of these difficulties are removed in granular solids, where the ultrafine metal particles are protected by, and uniformly dispersed in, an immiscible medium. The key feature of granular solids is that their properties hinge crucially on their nanostructure, characterized by the metal volume fraction (x_v) and the metal particle size ($2r$). By varying these nanostructure parameters, their physical properties can be greatly altered and tailored.

There are two types of granular metal solids, both of which are two-component systems. Granular metal embedded in an insulating medium, such as SiO_2 and Al_2O_3, have been known since the 1970s (4, 5). More recently, granular metal embedded in an immiscible metallic medium have been realized (9–12). The latter materials have led to the observation of, among other properties, giant magneto-transport phenomena. There is a rich variety of subjects in granular metal solids (4, 5), and we limit our discussions to some essential aspects of their magnetic and magneto-transport properties.

NANOSTRUCTURE

The intricate nanostructure of granular solids can be usefully, although only partially, described by two parameters. The first is x_v whose values can be continuously varied from 0 to 1. The second parameter, is $2r$, which is useful when isolated particles exist for samples with low values of x_v. The particle size can also be experimentally varied to a significant extent

through process conditions. In Figure 1, the evolution of the microstructure of granular solids (e.g. Ag-Al_2O_3, Fe-SiO_2) by varying x_v alone is depicted, and only the metal particles are shown. For all granular metal solids with a uniform dispersion of particles, a well-defined percolation volume fraction (x_p) exists, that has been experimentally observed (4, 5, 13) and theoretically understood (14) to be in the vicinity of $x_p = 0.5$–0.6. Isolated metal granules exist for $x_v < x_p$, and a continuous network of connecting granules appear for $x_v > x_p$. All characteristics of the nanostructure of granular metal solids, and indeed the variation of their physical properties, are intimately related to the particle size ($2r$) and the metal volume fraction (x_v).

Once x_v and $2r$ are defined, other structural characteristics of granular solids can be related. In real granular solids, the particles are not spherical but equiaxial, with a narrow size distribution, but not monodispersive. For simplicity, let us consider the ideal situation where all the particles are monodispersive spherical particles of radius r, randomly and uniformly distributed in a medium. Under these simplifications, one can easily calculate that the number of metal particles per volume is

$$n \approx \frac{1}{4}\frac{x_v}{r^3}. \qquad 1.$$

The interface area per volume, which is proportional to the surface to volume ratio of the particles, is

$$S \approx \frac{3x_v}{r}. \qquad 2.$$

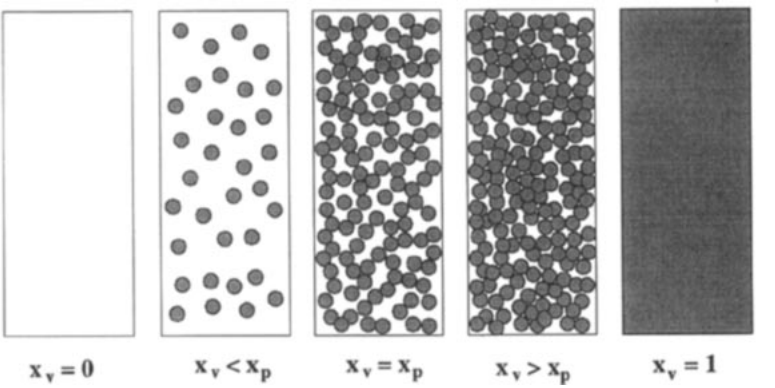

Figure 1 Schematic representations of granular metal-insulator solids as a function of metal volume fraction ($0 \leq x_v \leq 1$) with a percolation volume fraction (x_p).

The average particle–particle distance (from center to center) is

$$d \approx \left(\frac{16}{x_v}\right)^{1/3} r. \qquad 3.$$

At $x_v = 0.25$, $d \approx 4r$; i.e. the average spacing between the particles is about the size of the particle. These quantities will have relevance to the magnetic properties and the giant magneto-transport properties. It is also straightforward to show that, as long as the particles are randomly distributed, the metal area fraction (x_a) at the surface is the same as the metal volume fraction (x_v).

$$x_a = x_v. \qquad 4.$$

Thus the metal area fraction, as determined from the surface using microscopy, gives the value of the metal volume fraction.

Many physical properties undergo tremendous change as one varies x_v, particularly across x_p. Indeed, all physical properties whose characteristic lengths (e.g. coherent length in superconductors, critical size for single-domain magnetic particles, electron mean free path in transport properties, spin diffusion length in magneto-transport properties) are comparable to, or smaller than, the length scales inherent to a granular solid with certain values of x_v and $2r$ will be unavoidably affected. Most interesting of all, some of the enhanced physical properties can only be captured in granular solids and not in bulk materials. The enhanced magnetic properties and giant magneto-transport properties covered in this article are some of the examples discovered in recent years.

FABRICATION METHODS

Crucial to the formation of a granular solid is the fact that the two components must be immiscible; otherwise, a homogeneous alloy would be formed instead. At present, a number of methods can be used to prepare specimens that contain isolated ultrafine metallic particles of various sizes under 1000 Å. Examples include chemical precipitation (15–17), spark erosion (18), a high-energy ball milling (19), evaporation in an inert gas atmosphere (6, 20), and sol-gel method (21). However, it is a formidable task to prevent the ultrafine metal particles from oxidation and to disperse them uniformly into a suitable and protective medium. Furthermore, none of these methods can fabricate metallic entities in the nm scale with a narrow size distribution. To date, vapor deposition (particularly high-rate sputter deposition) of a metal and an immiscible material has proven to be the most versatile method of fabricating granular metal solids because

the formation of the nm-size particles, the protection of the vulnerable metal particles, the uniform dispersion of the particles, and coating onto desired surfaces are accomplished simultaneously (4, 5, 13). Existing results show that the metal particles may be elemental metals (e.g. Fe, Co, Ag) (4, 5, 13), crystalline alloys (e.g. Fe-Ni alloys) (22), metastable crystalline alloys (e.g. Fe-Cu) (22), or amorphous alloys (e.g. Fe-BN).

In the fabrication of granular metal solids using vapor deposition, x_v is determined by the composition. The particle size ($2r$), which depends to some extent on x_v (larger particles for higher values of x_v), can also be altered by processing conditions, of which substrate temperature is one of the most effective (13, 23). There are a number of variations within vapor deposition, and we illustrate these variations by applying to the fabrication of granular Fe-Al_2O_3.

1. Co-deposition from two separate sources (4, 5): The two sources (Fe and Al_2O_3) are directed toward the substrate. The contents of the two components are controlled by the relative deposition rates. With a slight variation in co-deposition, one can also achieve a gradient in composition across a large substrate and effectively obtain many small samples of different compositions [i.e. $Fe_x(Al_2O_3)_{1-x}$] (4). The drawback of co-deposition is that uniform composition exists only over small areas.
2. Tandem deposition from two separate sources (24): In this method, the two sources (Fe and Al_2O_3) are not directed at a common point. Instead, the substrate is moved rapidly over the two separate sources such that the accumulation of each material is small. However, because the deposition is sequential it is in fact the same scheme as that of fabricating a multilayer. Consequently, the composition is intrinsically non-uniform in the growth direction as is the dispersion of the particles. One immediate consequence of the non-uniform dispersion of the particles is that the percolation threshold is often much higher than the value of $x_p \approx 0.55$, which has been generally observed in granular samples with a uniform dispersion of particles (25).
3. Sputtering from a single composition target (4, 5, 13, 22, 23): This method relies on a uniform flux of the same composition over a large substrate area. It can most easily be administered using sputtering by taking advantage of the steady-state sputtering yield (26). Because sputtering sources can be readily scaled up (from a few cms to as large as a meter in size), sputtering is the preferred method for obtaining coatings of homogeneous composition over large surface areas. The drawback of this method is that one composite target has to be prepared for each composition.

4. Phase separation of immiscible metal (9–12): Recently, another method has been devised for the fabrication of metallic particles embedded in a metallic medium by taking advantage of the nearly complete immiscibility between two metals, such as Co-Ag, Co-Cu, and Fe-Ag (27, 28). Using a vapor-quenching method, metastable alloys of immiscible alloys can be readily formed. Annealing a metastable alloy at elevated temperatures induces phase separation, which causes the formation of metallic granules in a metallic medium (9–12). The size of the granules is dictated by the temperature and duration of the anneal. Alternatively, one can also form such granular metal-metal solids by deposition onto a substrate maintained at elevated temperatures.

CHARACTERIZATIONS

Characterization is obviously an integral part of any study of granular solids. Because the intricate structure exists on the nanometer scale, only characterization tools with nm-scale resolution will be useful. The main pieces of information that one wishes to extract from granular solids are purity, structure and phases of the constituent components, $2r$ and its distribution, x_v, and the connectivity of the particles. Some of the methods reported in the literature are X-ray diffraction (XRD), both large-angle and small-angle, transmission electron microscopy (TEM), electron diffraction, X-ray photoelectron spectroscopy (XPS), neutron diffraction (especially for magnetic granular solids), and ^{57}Fe Mössbauer spectroscopy (for granular solids containing Fe). For magnetic granular solids, magnetometery measurements can also shed light on the size of the magnetic particles. Of those, the most useful, and consequently, the most widely used techniques, are XRD and TEM. We briefly describe those results here.

Of the two types of granular solids, the characterization of the nanostructure of granular metal-insulator solids (e.g. Fe-Al_2O_3) are generally more clear-cut than those of granular metal-metal solids. This is because the insulating medium is often amorphous (thus largely featureless in XRD and TEM), and therefore the metal particles stand out (4, 5, 13). Large-angle and small-angle XRD patterns of granular Fe-Al_2O_3 ($x_v = 0.35$) are shown in Figure 2. The large-angle pattern (*left*) clearly shows that the ultrafine Fe particles are crystalline with a body-centered cubic (bcc) structure. The broad diffraction line width is a consequence of the small particle size. In the small-angle XRD pattern shown on the right, there is a distinct minimum at the scattering vector $S = 0.15$ Å due to the particles of size $2\pi/S = 42$ Å. The minimum can only be observed from granular

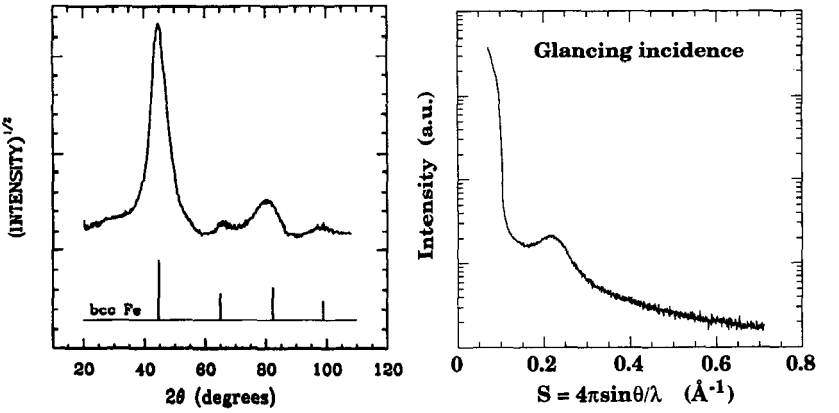

Figure 2 Large-angle and small-angle X-ray diffraction patterns of Fe-Al_2O_3 ($x_v = 0.35$). The large-angle pattern shows the bcc structure of Fe, whereas the small-angle pattern shows a minimum at S ≈ 0.15 Å due to particles with a narrow distribution of size $2\pi/S \approx 42$ Å.

solids with a narrow size distribution (J Jiang & C Chien, unpublished data).

Examples of TEM micrographs of granular metal-insulator solids, specifically ($Fe_{50}Ni_{50}$)-(SiO_2) ($x_v = 0.4$) deposited at $T_S = 150°C$ (22) (*upper panel*), and Co-SiO_2 with $x_v = 0.12$, 0.22 and 0.51 (A Tsoukatos & G Hadjipanayis, unpublished data) (*lower panel*) are shown in Figure 3. The

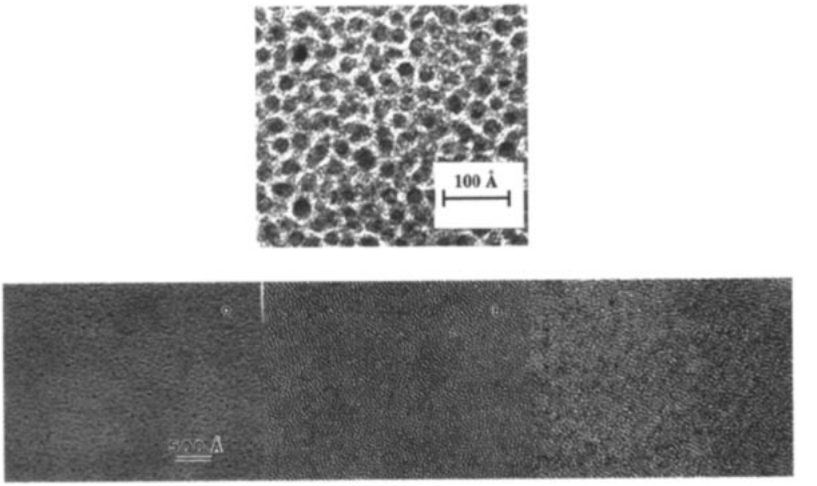

Figure 3 Transmission electron micrographs of $Fe_{50}Ni_{50}$-(SiO_2) ($x_v = 0.4$) deposited at $T_A = 150°C$ (*upper panel*), and Co-SiO_2 with (*a*) $x_v = 0.12$, (*b*) $x_v = 0.22$ and (*c*) $x_v = 0.51$ (*lower panel*).

amorphous insulator is the light featureless background, and the dark entities are the metals. Particles of about 40 Å in size (*upper panel*), with a narrow distribution of sizes, are clearly observed. The TEM micrographs on the lower panel also illustrate the fact that the particle size increases with increasing x_v. The TEM micrograph for $x_v = 0.51$ on the lower panel is at the verge of percolation; hence the particles are connected to a large network.

Characterization of granular metal-metal solids (e.g. Co-Cu) are more difficult because both components are crystalline with small grain sizes, and with poorer TEM contrast (10, 29). To complicate matters further, the XRD and electron diffraction patterns of the two components may have overlapping diffraction lines. Bright-field TEM micrographs and electron diffraction patterns of $Co_{20}Ag_{80}$ are shown in Figure 4. The diffraction rings of face-centered cubic (fcc) Co and fcc Ag are also labeled (31). In the as-prepared sample (a), deposited at $T_S = 77$ K, all the diffraction rings match those of bulk Ag, confirming the formation of a metastable fcc alloy. The broad Ag(111) rings result from the small grains, which are about 4 nm in size. After annealing (b), (c), and (d), the grain size becomes larger as expected. No clear-cut diffraction rings corresponding to fcc Co are discernible for the sample annealed at $T_A = 200°C$ [with the caveat that the Co(111) and Ag(200) rings are overlapping]. The results for the samples with $T_A \geqslant 330°C$ show that phase separation has definitely occurred and the particles are larger for higher value of T_A. Converging beam measurements show that each particle is of one element, surrounded by particles of the second element (32).

MAGNETIC PROPERTIES

Strongly ferromagnetic materials may not necessarily have hard magnetic properties that are required for permanent magnet and magnetic recording applications. Metallic Fe has one of the highest saturation magnetizations (M_s) and the second highest Curie temperature (T_C). But the magnetocrystalline anisotropy energy constant (K) is quite small, so that multiple domains with closure-domain structure readily formed in bulk Fe (23). As a result, bulk Fe is magnetically soft with low coercivity (H_c) of the order of 10 Oe. The situation takes a dramatic turn for ultrafine magnetic particles (33, 34). Because the domain walls have a finite thickness (of the order of a few hundred Å), when the magnetic particle is sufficiently small, only one magnetic domain can be formed. In a single-domain magnetic particle, all the magnetic moments are aligned and rotate in unison under an external field as a giant moment, resulting in hard fer-

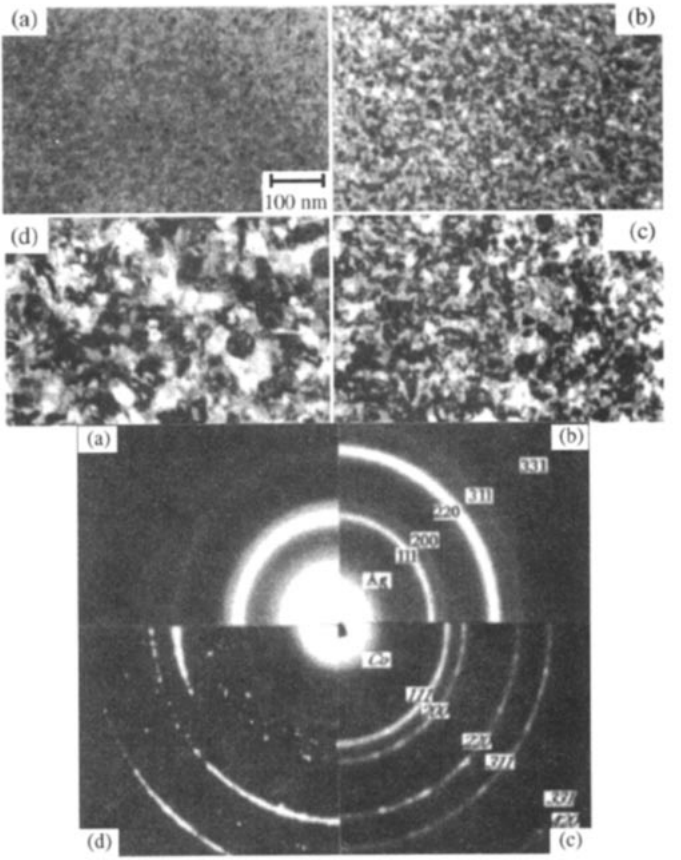

Figure 4 Bright-field transmission electron micrographs (*upper panel*) and electron diffraction patterns (*lower panel*) of $Co_{20}Ag_{80}$ samples deposited at 77 K and after annealing at various temperatures (T_A): (*a*) as-prepared, (*b*) $T_A = 200°C$, (*c*) $T_A = 330°C$, and (*d*) $T_A = 605°C$. In the lower panel, the electron diffraction patterns for fcc Ag and fcc Co are labeled.

romagnetic characteristics. The critical sizes for the formation of single domain for Fe, Co, and Ni are of the order of a few hundred Å, depending on the material and shape of the particle (33, 34). Particles of such small sizes, while challenging for traditional material synthesis, can be readily accomplished in granular magnetic solids. In granular solids, one observes the magnetic behavior of single-domain magnetic particles and the associated phenomenon of superparamagnetism in samples with low volume fractions ($x_v < x_p$). Bulk magnetic properties are recovered in samples with $x_v > x_p$.

Single-Domain Characteristics

In a granular magnetic solid with a low volume fraction, one has a collection of single-domain particles (4, 5, 13, 35, 36), each with a magnetic axis along which all the moments are aligned. In the absence of a magnetic field, parallel and antiparallel orientations along the magnetic axis are energetically equivalent but separated by an energy barrier of CV, where C is the total magnetic anisotropy per volume, and V is the particle volume. Since the size of each single-domain remains fixed, under an external field, only the magnetic axes rotate. Thus, the measured magnetization (M) of a granular magnetic solid with a collection of single-domain particles is the global magnetization

$$M = \frac{\langle \mathbf{M} \cdot \mathbf{H} \rangle}{H} = M_s \langle \cos\theta \rangle, \qquad 5.$$

where θ is the angle between the magnetic axis of a particle, M_s is the saturation magnetization, $\mathbf{H}$ is the external field, and the average $\langle \cos\theta \rangle$ is taken over many ferromagnetic particles. The hysteresis loop of a granular solid is a signature of the rotation of the magnetic axes of the single-domain particles. This should be contrasted with the hysteresis loop of a bulk ferromagnet, in which the sizes and directions of the domains are altered drastically under an external field (33).

An example of a hysteresis loop of a granular magnetic solid at low temperature is shown in Figure 5*a*. In the initial unmagnetized state with $M = 0$ at $H = 0$, the magnetic axes of the particles are randomly oriented, each along its own magnetic axis, which is determined by the total magnetic anisotropy of the particle. The directions of the giant moments are random and static at low temperatures. A saturation magnetization ($M = M_s$) is realized under a large field when all the magnetic axes are aligned. In the remnant state when H is reduced to $H = 0$, one observes the remnant magnetization (M_r), whose value at low temperature is $M_r = M_s/2$. This is because the magnetic axes are oriented only in one hemisphere due to the uniaxial anisotropy of the single-domain particle (13, 36).

It should be noted that the initial $M = 0$ state and the initial magnetization curve in Figure 5*a* does not reappear, whereas the field-cycle part does. The simplest way to recover the initial $M = 0$ state is to heat the sample above the blocking temperature (see below) and cool the sample in zero field back to low temperatures.

Because of the single-domain nature of the magnetic entities, the coercivity (H_c) of the ultrafine particles is expected to be much higher than that in bulk material. For free-standing spherical single-domain Fe particles, theoretical studies indicate a coercivity of $2K/M_s = 600$ Oe (37–39), which

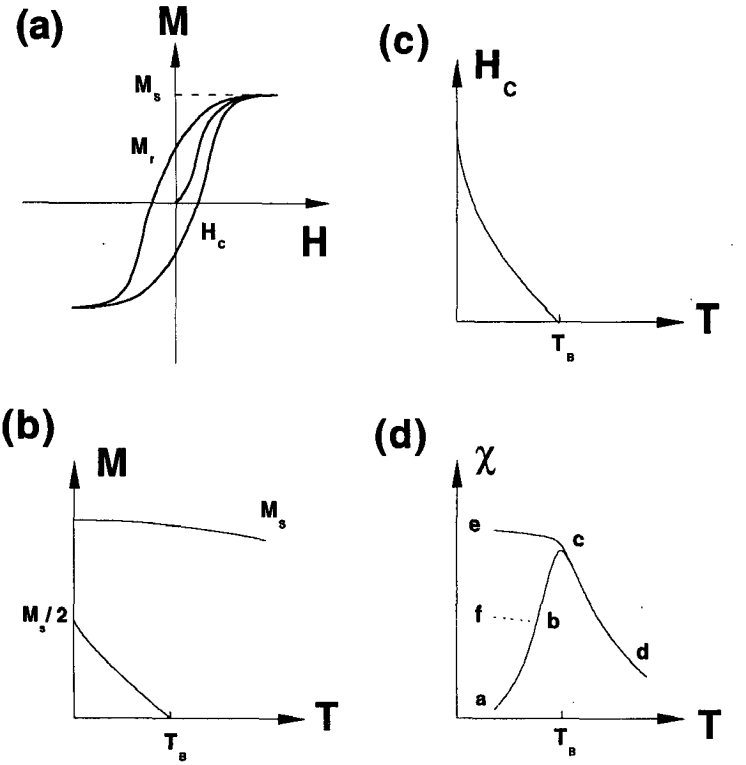

Figure 5 (*a*) Hysteresis loop at 5K; (*b*) temperature dependence of saturation magnetization (M_s) and remnant magnetization (M_r); (*c*) temperature dependence of coercivity (H_c); (*d*) temperature dependence of field-cooled (FC) and zero-field–cooled (ZFC) susceptibility. At the blocking temperature (T_B), M_r and H_c vanish, whereas the ZFC susceptibility shows a cusp-like feature.

is much larger than the 10 Oe value observed for bulk Fe. Many granular Fe-insulator solids actually exhibit even larger coercivities, to as much as 3000 Oe at 5 K and 1100 Oe at 300 K (13, 36, 40, 41). This is due in part, as described below, to the very large total magnetic anisotropy constant (C). The value of C includes magnetocrystalline anisotropy (K) and other contributions that dominate in granular Fe embedded in a medium, so that $C \gg K$. Some researchers have suspected the role of possible metal-oxide shells surrounding the Fe particles to account for the exceptionally large values of coercivity. Evidences of metal oxides have been suggested by XPS and some Mössbauer measurements (25, 42, 43). However, many granular metal–metal systems (e.g. Co-Ag, Fe-Cu, Fe-Ag) also have very large coercivity up to 3000 Oe, but without the presence of oxides (10, 11,

44). The large values of coercivity of granular solids, together with smaller recording noise intrinsic to small particles systems, suggest applications as magnetic recording media (40, 41). However, the anomalously large coercivity, the large total anisotropy constant (C), and the particle size dependence of H_c (H_c increases with particle size) (23) remain as some of the outstanding issues.

Superparamagnetic Relaxation

At sufficiently high temperatures, the energy barrier (CV) is overcome by the thermal energy (4, 5, 13, 33–36, 45–47). Consequently, the magnetic moments within a particle rotate rapidly in unison, exhibiting the well-known superparamagnetic relaxation phenomenon. The simplest form of the relaxation time can be described by the Arrhenius relation (33)

$$\tau = \tau_0 \exp(CV/k_B T), \qquad 6.$$

where τ is the relaxation time, τ_0 is the characteristic time, and CV is the total anisotropy energy. For an instrument that can measure certain magnetic characteristics (e.g. magnetometery, AC susceptibility, Mössbauer spectroscopy) with a measuring time of τ_i, one can define a blocking temperature

$$T_B = \frac{CV}{k_B \ln(\tau_i/\tau_0)}. \qquad 7.$$

At $T < T_B$, τ_i is less than τ and the instrument detects the ferromagnetic nature (e.g. a hysteresis loop) of the system. However, at $T > T_B$, because τ_i is longer than τ, the time averaged values of the ferromagnetic characteristics (e.g. magnetization and coercivity) vanish within the measuring time of τ_i. The system is in an apparent paramagnetic or superparamagnetic state, even though within each particle the magnetic moments remain ferromagnetically aligned. Because of superparamagentic relaxation, the values of remnant magnetization (M_r) and coercivity (H_c) decrease with increasing temperature and vanish at the blocking temperature (T_B) (13, 36, 45). Above T_B, all apparent ferromagnetic characteristics disappear. These aspects are shown in Figure 5*b* and *c*.

Another useful technique for the measurement of superparamagnetic relaxation is low-field susceptibility measurements in both zero-field-cooled (ZFC) and field-cooled (FC) modes (36). As shown in Figure 5*d*, above T_B, the FC and ZFC data are the same and hence reversible. Below T_B, however, the FC and ZFC data are totally different and irreversible. In particular, the ZFC data shows a readily detectable cusp-like feature at

T_B. The requirement of a low field is necessitated by the fact that Equation 6 is defined in the limit of $H = 0$ (36). Low-field susceptibility has been widely used by many people to provide evidence for the existence of ultrafine magnetic particles and/or superparamagnetism. However, it must be emphasized that the irreversibility of the ZFC and the FC branches, and the cusp-like feature of the ZFC branch are also tell-tale signs of spin-glass transitions and often appear even in ferromagnets (e.g. Gd). Another important, but often overlooked technical point is that T_B can be located from the ZFC branch only when the reversible part has been reached (for example, in Figure 5(*d*), $a \rightarrow b \rightarrow c \rightarrow d \rightarrow c \rightarrow e$). An apparent irreversibility is observed when increasing temperature is reversed to decreasing temperature during a measurement (for example in Figure 5(*d*), $a \rightarrow b \rightarrow f$), before the actual T_B is reached. This may occur, for example, when the limit of the accessible temperature has been reached. The temperature that corresponds to point *e* is not T_B.

It should be noted that superparamagnetic relaxation is a time effect (4, 5, 13, 33–36, 45–47). Therefore, the best methodology for ascertaining superparamagnetism is to employ two or more instruments with widely different measuring times. The same sample reveals different superparamagnetic relaxation effects when viewed by instruments with different measuring times—one blocking temperature (T_{Bi}) for each instrument with a specific measuring time τ_i, as defined by Equation 7. Thus by using two or more instruments of very different measuring times (36), or by conducting AC measurements over a wide frequency range (46), one can firmly establish superparamagnetism relaxation. For example, using SQUID magnetometery ($\tau_i \approx 10$ s) and Mössbauer spectroscopy ($\tau_i \approx 10^{-8}$ s), for two measured blocking temperatures have the same ratio of 0.35, regardless of the samples (36).

Furthermore, using more than one instrument with very different measuring times, one can also separately determine CV and τ_o. Together with an independent measurement of V (e.g. microscopy), the value of C can be determined (36). It has been found in many ultrafine single-domain magnetic particles that the values of C are much larger than the magnetocrystalline anisotropy energy densities of the constituent magnetic materials in bulk form, some by as much as two orders of magnitude (13, 36, 40, 42, 46, 47). For example, while the magnetocrystalline anisotropy energy constants are $K \approx 10^5$ erg/cm^3 and 10^4 erg/cm^3, respectively, for bulk Fe and $Fe_{50}Ni_{50}$, much larger values of C, in excess of 10^7 erg/cm^3, have been observed in granular Fe-SiO_2 and ($Fe_{50}Ni_{50}$)-(Al_2O_3) (22, 36, 47). Evidently, mechanisms other than magnetocrystalline anisotropy are the dominant factors for the large magnetic anisotropy in ultrafine magnetic particles embedded in a matrix. This enhancement of C in part

accounts for the very large coercivities observed in granular magnetic solids as mentioned above.

It may be noted from Equation 7 that the value of T_B is proportional to the volume (V) of the particle, hence proportional to r^3. Even a modest increase in $2r$ (e.g. a factor of 3) can result in hundreds of degrees of increase in the value of T_B (22). Indeed, by controlling the particle size through process conditions, one can vary the value T_B from less than 10 K to several hundred degrees above room temperature.

Finally, we comment on the validity of the Arrhenius relation (Equation 6) for the relaxation time. Because of its simplicity, it has been widely used, especially if one has only one measuring instrument so that the value of τ_0 must be assumed (most often τ_0 is taken to be about 10^{-9} s) in order to extract the value of CV. On the other hand, measurements with two or more instruments, where one can determine both τ_0 and CV by using the Arrhenius law, concluded a wide range of values for τ_0, from 10^{-9} to 10^{-25} s (13, 36, 46). The extremely short values of $\tau_0 < 10^{-15}$ s clearly must be artifacts. This dilemma can be understood as follows. Extensive measurements of the relaxation time using SQUID magnetometery ($\tau_i \approx 10$ s) (36), AC susceptibility ($\tau_i \approx 10^{-4}$–10^{-1} s) (46), Mössbauer spectroscopy ($\tau_i \approx 10^{-8}$ s) (36, 47), and small-angle neutron diffraction ($\tau_i \approx 5 \times 10^{-12}$ s) (48) indicate that the actual relaxation time does not strictly follow an Arrhenius relation. As schematically shown by the plot of $\ln\tau$ vs $1/T$ in Figure 6, the results from magnetometery, AC susceptibility, and Mössbauer measurements fall on a curve rather than a straight line. Small-angle neutron diffraction measurements indicate that the value of τ_0 is likely to be near 10^{-11} s (24). As shown in Figure 6, if SQUID magnetometery and Mössbauer spectroscopy were used, a straight line Arrhenius relation would give $\tau_0 \approx 10^{-13}$ s (36), whereas if AC susceptibility results were used, the straight line would give $\tau_0 \approx 10^{-19}$ s (46).

Superparamagnets with Giant Moments

At $T > T_B$, the magnetic particles exhibit superparamagnetic characteristics of a paramagnetic system of giant moments. The magnetization behavior (i.e. M vs H) follows that of a Langevin function for classical magnetic moments (33),

$$\frac{M}{x_v M_s} = L\left(\frac{\mu H}{k_B T}\right) = \coth\left(\frac{\mu H}{k_B T}\right) - \frac{k_B T}{\mu H}, \qquad 8.$$

where $\mu = M_s V$ is the giant magnetic moment (about 10^4 μ_B) of a single particle with volume V, and H is the external field. In suitable ranges of

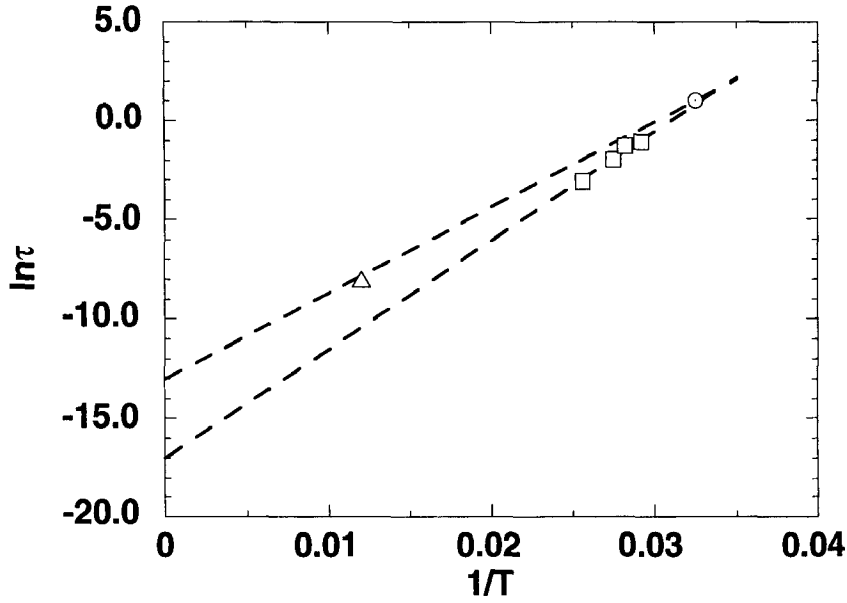

Figure 6 Semi-log plot of relaxation time (τ) as a function of $1/T$. Results from magnetometery (M) and Mössbauer effect (ME) are denoted by circle and triangle respectively. The AC susceptibility (AC) results are denoted by squares. The two dashed straight lines assumed Arrhenius relation linking the results of M and ME, as well as extrapolating linearly the AC results.

temperature and magnetic field, the Langevin function depends sensitively on the value of μ, and hence the particle size, (V), as shown in Figure 7. A detailed analysis of the magnetization behavior permits the determination of the values of the giant moments (49). This information can, in turn, be converted to particle sizes.

At $T > T_B$, the magnetic susceptibility behaves as (49)

$$\chi = \frac{x_v V M_s^2(T)}{3k_B(T-T^*)}. \qquad 9.$$

This form, which follows from Equation 8, is very similar to the well-known Curie-Weiss susceptibility of a paramagnet (33),

$$\chi = \frac{n[g\mu_B J(J+1)]^2}{3k_B(T-\theta)}, \qquad 10.$$

where n is the number of the effective magnetic moment $g\mu_B J(J+1)$, and θ is the Curie-Weiss constant, which is a measure of the strength of the

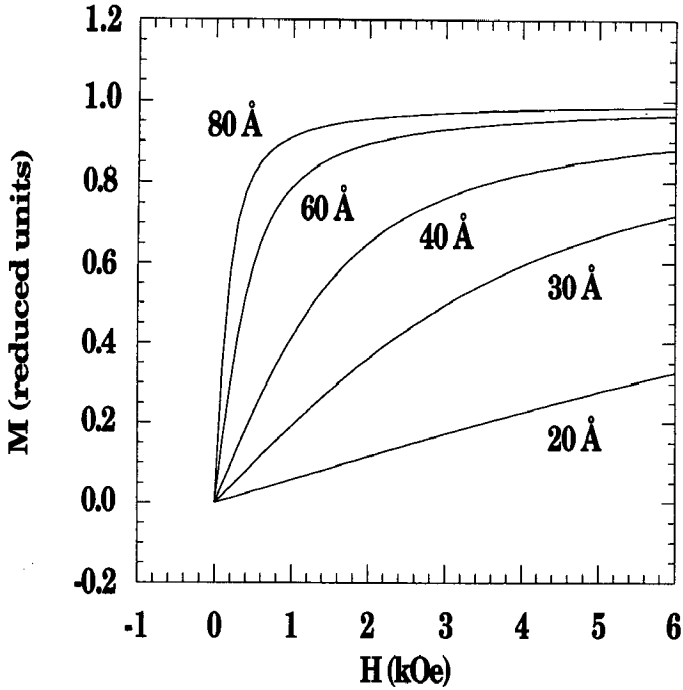

Figure 7 Calculated magnetization behavior at $T = 300$ K of Fe particles of various sizes.

magnetic interactions among the moments (33). The key difference is that the giant moment is about 10^4 times larger than the individual atomic moment. The analyses of the susceptibility data offer still another means of measuring the giant moments and hence the particle sizes. The quantity T^*, the analogue of the Curie-Weiss temperature of a paramagnet, provides a measure of the interaction among the superparamagnetic giant moments (50). In most cases, T^* is of the order of 20 K, suggesting weak inter-particle interactions (49). It should also be noted that the effective magnetic moment in Equation 10 is a constant, thus $1/\chi$ in a paramagnetic system is linear in T. For a granular system, $M_s(T)$ in Equation 9 is temperature dependent, hence the $1/\chi$ plot in a granular system is not linear in T. This fact can be used for the purpose of measuring the temperature dependence of $M_s(T)$ of a superparamagnetic particle, which otherwise is not easily accessible in magnetometery measurements (49).

The giant moments of a superparamagnet can be exploited in magnetocaloric applications. Recently, the utility of granular magnetic solids has been demonstrated in magnetic refrigeration (51), where the giant

moments provide higher efficiency and a higher operating temperature range over those of conventional paramagnetic materials.

GIANT MAGNETO-TRANSPORT PROPERTIES

When a material is subjected to an external field, currents of charge or energy may flow. These responses to applied fields are the transport properties, which provide valuable information of the material. The applied fields may be electric, magnetic, thermal gradient, or a combination thereof. Although the specific transport property may involve only one external field, such as electrical resistivity (electric field), more interesting effects may occur when two fields are applied simultaneously, such as magnetoresistivity and Hall resistivity (electric field and magnetic field), and magneto-thermal conductivity (thermal gradient and magnetic field). Each transport property reveals certain information concerning the material in which it occurs. Magnetoresistivity provides a measure of the scattering events contributing to the magnetic resistivity. Thermal conductivity reveals the relative importance of large-angle and small-angle scattering events, as well as that of elastic vs inelastic events.

While the overwhelming majority of studies of giant magneto-transport properties has centered on magnetoresistance, especially in multilayers (52–62), magnetoresistivity is but one of several transport properties, all of which are essential for the understanding of the magneto-transport properties in magnetically heterogeneous systems of multilayers and granular solids. In this section, we describe the main features and the outstanding issues of the giant magneto-transport properties of granular metal systems, including magnetoresistivity, extraordinary Hall resistivity, and magneto-thermal conductivity.

When a specific transport property, for example, electrical resistance (in units of Ω) is measured from a material, its value depends on the resistivity (ρ in units of $\mu\Omega$-cm) as well as the physical dimensions of the specimen. In order to understand the scattering processes that contribute to this transport property, one must determine the absolute value of ρ, by also measuring the physical dimensions of the specimen. If the physical dimensions of the specimen are unknown, one can, at most, measure the changes of the transport property by expressing them in a fraction form (i.e. $\Delta R/R = \Delta\rho/\rho$). Without knowing the value of ρ, one is in no position to seek the physics that causes the observed fractional change. The physics that gives rise to an effect of $\Delta R/R = \Delta\rho/\rho = 20\%$ when ρ is in the $\mu\Omega$-cm range is entirely different from that when ρ is in the mΩ-cm range. In the following descriptions of the transport properties, we discuss the measured transport properties in absolute values of resistivity and conductivity.

MAGNETORESISTIVITY (ρ_{xx})

Magnetoresistance (MR) is the variation of electrical resistance due to an external magnetic field (**H**) (63). Positive or negative MR refers to the increase or decrease of resistance with the magnetic field. For thin-film specimens, where the electric current with a current density (**j**) is usually in the film plane, MR can be measured in three geometrices: $\boldsymbol{\rho}_{\parallel}$ (longitudinal MR, $\mathbf{H}\|\mathbf{j}$), $\boldsymbol{\rho}_{T}$ (transverse MR, **H** is in the film plane and perpendicular to **j**), and $\boldsymbol{\rho}_{\perp}$ (perpendicular MR, **H** is perpendicular to the film plane and perpendicular to **j**), as shown in Figure 8. It is generally necessary to measure MR in more than one field orientation to ascertain its characteristics.

For a Drude metal of free electrons, there is no MR, i.e. resistance is independent of H, as shown in Figure 9*a*. The characteristics of MR in various real materials at low temperatures can be summarized as follows—roughly in increasing order of the size of MR effect size:

1. Ordinary magnetoresistance (OMR): For ordinary non-magnetic metals, such as Au and Cu, the MR is quite small. Both $\boldsymbol{\rho}_{\parallel}$ and $\boldsymbol{\rho}_{T}$ are

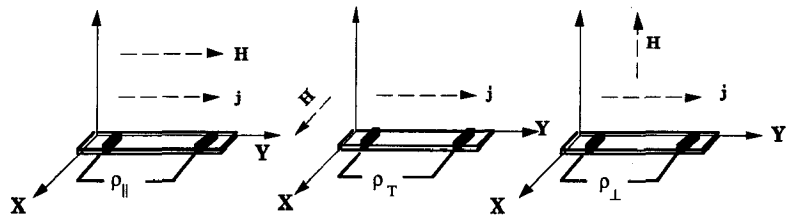

Figure 8 Longitudinal magnetoresistivity ($\rho_{\parallel}$), transverse magnetoresistivity (ρ_T), and perpendicular magnetoresistivity ($\rho_{\perp}$) measured in an external magnetic field (**H**) applied in different direction with respect to a current, with current density (**j**) flowing in the plane of the thin-film sample.

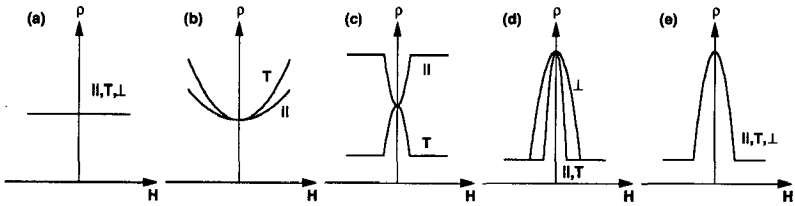

Figure 9 Schematic representation of various magnetoresistance (MR) behaviors: (*a*) the absence of MR in a Drude metal, (*b*) ordinary MR in a non-magnetic metal, (*c*) anisotropic MR in a ferromagnetic metal, (*d*) negative giant MR in a multilayer, and (*e*) negative giant MR in a granular solid.

positive and increase unabated as H^2, with $\rho_T > \rho_\parallel$, as shown in Figure 9*b*.

2. Anisotropic magnetoresistance (AMR): In ferromagnetic metals (e.g. Fe, Co) and alloys (e.g. permalloy), substantial MRs are observed. It is almost always the case that $\rho_\parallel$ is positive and ρ_T is negative, as shown in Figure 9*c*, and $\rho_\parallel > \rho_T$, which is opposite to that of OMR. Both $\rho_\parallel$ and ρ_T can be saturated under a modest field. The AMR depends on the direction of the spontaneous magnetization and is due to the rotation of the ferromagnetic domains under the external field (64). The saturation field (H_s) for the AMR in permalloy is especially small (less than 10 Oe). This, together with the sizable values of $\Delta\rho \approx 0.5$ $\mu\Omega$-cm and $\Delta\rho/\rho_{avg} \approx 2\%$ at room temperature, forms the basis for most low-field magnetoresistive applications (64).
3. Giant magnetoresistance (GMR) in magnetic multilayers: In 1988, Baibich et al (52) discovered giant negative magnetoresistance in Fe/Cr multilayers with certain Cr layers thicknesses through which the interlayer exchange interaction (J) caused antiferromagnetic alignment of adjacent Fe layers, leading to zero magnetization ($M = 0$) (52, 53). Under a sufficiently large magnetic field, a ferromagnetic alignment ($M = M_s$) was achieved. Remarkably, the resistivitiy between the ferromagnetic and the antiferromagnetic alignments differed by as much as a factor of two. Subsequently, such large MR effects and the intricate oscillations in MR, as caused by the oscillatory J, have been observed in a large variety of multilayers (54–62). Because the MR in Fe/Cr was so large, the MR effect has been widely referred to as giant magnetoresistance (GMR). Since the discoveries made in 1988, GMR and interlayer coupling have captured tremendous worldwide interest from many researchers. Prior to 1992, the attention has been focused exclusively on multilayers, upon which most theoretical models have also been based. In 1992, GMR was uncovered in granular magnetic systems, dispelling the notion that the GMR phenomenon is exclusive to multilayers (44, 65).

The GMR effects observed in multilayers and granular solids can indeed be quite large ($\Delta\rho/\rho \geqslant 50\%$) in some cases, but modest ($\Delta\rho/\rho < 5\%$) in others. But what distinguishes the GMR effect from other MR effects is not just the size of the effect, but its distinctively different characteristics. First of all, the GMR is always negative, i.e. resistance decreases with increasing field, irrespective of the direction of the applied magnetic field with respect to the current, as shown in Figure 9*d*. This is qualitatively different from the positive OMR observed in non-magnetic metals, and the positive and negative AMR observed in magnetic metals. Because of

the layer structure, GMR in multilayers is not isotropic (52); specifically $\rho_\perp > \rho_\parallel \approx \rho_T$, as shown in Figure 9*d*. Furthermore, other characteristics of GMR in granular solids, as described below, are also different from those of ordinary metals and alloys.

OMR, AMR, and GMR are not isolated effects. AMR is also present in systems that exhibit GMR. This is of particular concern if the GMR is quite small. In such cases, measurements must be extended to several geometries to separate out the AMR contribution (60). Under a large magnetic field, AMR materials often display a weak H^2 dependence due to OMR (64).

The first observation of GMR in granular materials was independently made and simultaneously published by Berkowitz et al (65) and Xiao et al (44), using granular Co-Cu samples after Childress and Chien reported the fabrication of granular Co-Cu (10, 11). Barnard et al (66) observed unexpectedly large values of magnetoresistance in Co-Ag thin films, which probably contained some features of granular solids. Shortly thereafter, GMR was uncovered in a number of granular systems of Co, Fe, Ni, and their alloys embedded in noble metals (Ag, Cu, and Au) (29, 67–75).

In Figure 10*a*, we show the megnetoresitance at 5 K of $Co_{16}Cu_{84}$ deposited at $T_S = 350°C$ (44). The apparent dependence of GMR on H is not particularly revealing because GMR is a direct consequence of the field dependence of the global magnetization (M). The highest and the lowest resistivities are realized respectively at the original unmagnetized state ($M = 0$) and when all the particles are ferromagnetically aligned ($M = M_s$). These two states correspond to the antiferromagnetic ($M = 0$) and ferromagnetic ($M = M_s$) alignments of multilayers. Shown in Figure 10*b* is the hysteresis loop, which closely correlates with the magnetoresistance curves. The increasing-field and the decreasing-field branches of MR correspond exactly to those of the hysteresis loop. The maxima of MR are located precisely at the coercive fields. The correlation between the MR and global magnetization is clearly shown in Figure 10*c*, which is a replot of Figure 10*a*,*b* using the data at the same H. The relationship reveals that the GMR is an even function of the global magnetization (M) (29). It should be noted in Figure 10*a* and *b* that the initial curve ($a \rightarrow b$) is not reproducible under field cycling, and only the field-cycle parts ($b \rightarrow c \rightarrow d \rightarrow e \rightarrow b$) can be used for the correlation shown in Figure 10*c*.

Although GMR data have often been described in percent ($\Delta\rho/\rho$), it is the absolute resistivity values of ρ and $\Delta\rho$ that contain the intricate physics. It has been found in granular magnetic systems exhibiting GMR that the essential physics is contained in the resistivity of the form of (29, 69)

$$\rho(H, T) = \rho_0(T) + \rho_m(T)[1 - F(M/M_s)], \qquad 11.$$

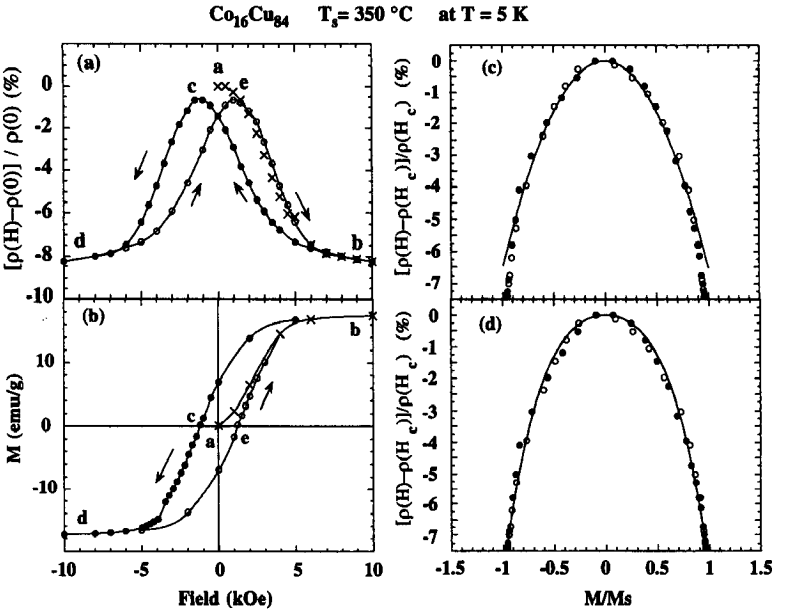

Figure 10 Magnetization (*a*) and hysteresis loop (*b*) of granular $Co_{16}Cu_{84}$ ($T_s = 350°C$) at 5 K. The crosses and closed and open circles denote the initial curve ($a \rightarrow b$), the branch with decreasing field ($b \rightarrow c \rightarrow d$), and the branching with increasing field ($d \rightarrow e \rightarrow b$), respectively. These two plots are combined in (*c*) and (*d*) to show magnetoresistance vs global magnetization. The solid curve in (*c*) is $\Delta\rho/\rho = -0.065\ (M/M_s)^2$, whereas the solid curve in (*d*) is $\Delta\rho/\rho = -0.0824\ [(1-\alpha)\ (M/M_s)^2 + \alpha\ (M/M_s)^4]$ with $\alpha = 0.5$.

where the first term $\rho_0(T)$ is the field-independent part of the resistivity due to the usual contributions from phonon, defect, and impurity scattering. The second term in Equation 11 is responsible for GMR. The value of the magnetic resistivity $[\rho_m(T)]$ in comparison with $\rho_0(T)$ determines the actual effect size of the GMR. The field dependence of $\rho(H, T)$ is through the field dependence of the global magnetization M via the function $F(M/M_s)$, where M_s is the saturation magnetization. The function $F(M/M_s)$ is an even function of M/M_s with the limiting values of $F(M/M_s) \rightarrow 0$ as $M \rightarrow 0$ (when $H = 0$ or H_c, where H_c is the coercive field) and $F(M/M_s) \rightarrow 1$ as $M \rightarrow M_s$ (when $H \geqslant H_s$, where H_s is the saturation field).

The experimentally observed size of the GMR, if expressed in percent and relative to the high resistance state, is just (69)

$$\left(\frac{\Delta\rho}{\rho}\right)_0 = \frac{\rho(0,T)-\rho(H_s,T)}{\rho(0,T)} = \frac{\rho_m(T)}{\rho_0(T)+\rho_m(T)}. \qquad 12.$$

The size so expressed will at most be 100% when $\rho_m(T) \gg \rho_0(T)$. Alternatively, the size of GMR can also be expressed as

$$\left(\frac{\Delta\rho}{\rho}\right)_{H_s} = \frac{\rho(0,T)-\rho(H_s,T)}{\rho(H_s,T)} = \frac{\rho_m(T)}{\rho_0(T)}, \qquad 13.$$

with respect to the low resistance state. The size can now be even greater than 100% when $\rho_m(T) > \rho_0(T)$. Not surprisingly, most results in the literature are expressed in the latter form to maximize the reported size. From Equations 12 and 13, it is clear that the size of the GMR depends on a combination of both $\rho_0(T)$ and $\rho_m(T)$, which must be separately measured.

Experimentally, it has been found that the function $F(M/M_s)$ can be well approximated by $F(M/M_s) \approx (M/M_s)^2$ (44) as shown in Figure 10*c*. In a granular system $(M/M_s)^2 = \langle\cos\theta\rangle^2$, where θ is the angle between the magnetization axis of a particle and the external field, and $\langle\cos\theta\rangle^2$ is averaged over many ferromagnetic particles. The physical significance of $(M/M_s)^2$ is, in the limit of uncorrelated particles $(M/M_s)^2 = \langle\cos\theta\rangle^2 = \langle\cos\phi_{ij}\rangle$, where ϕ_{ij} is the angle between the axes of the ferromagnetic particles, which highlights the importance of the relative orientation of the magnetic axes of the ferromagnetic particles (44). This can be readily seen as follows. Consider two ferromagnetic particles of magnetizations $\mathbf{M_i}$ and $\mathbf{M_j}$, then $\mathbf{M_i}\cdot\mathbf{M_j} = M_i M_j \cos\phi_{ij}$. Because z is the symmetry axis along which $\mathbf{H}$ is applied, $\langle\cos\phi_{ij}\rangle = \langle\cos\phi_i\cos\phi_j\rangle$. In the limit that the magnetic axes are uncorrelated, $\langle\cos\phi_{ij}\rangle = \langle\cos\phi_j\rangle^2 = (M/M_s)^2$, as experimentally observed. The description of the GMR data can be further improved by using $F(M/M_s) = (1-\alpha)(M/M_s)^2 + \alpha(M/M_s)^4$, where α is a fitting parameter with a value between 0 and 1, as shown in Figure 10*d*. The dependence of GMR on $(M/M_s)^2$ and other higher power terms accounts for the experimental fact that, under a magnetic field, the global magnetization always saturates faster than the GMR, as shown in Figure 10.

A key feature of GMR in granular systems, distinctively different from that in multilayers and AMR, is that the GMR in granular systems is isotropic (29), whereas both the AMR (64) and the GMR in multilayers (52) are inherently anisotropic. In a granular system that exhibits GMR, $\rho_\perp \approx \rho_\parallel \approx \rho_T$, as schematically shown in Figure 9*e*. Granular magnetic systems are the only magnetic media that show isotropic GMR. When used as a magnetoresistive field-sensing device, the field can be oriented in any direction with respect to the sample, whereas in both AMR alloy films (64) and GMR in multilayers (52), the magnetic field is required to be parallel to the film plane.

The magnetic resistivity (ρ_m), which dictates the size of the GMR as shown in Equations 12 and 13, depends on the particle size and the density of the ferromagnetic particles in a granular solid. The dependence of ρ_m on $2r$ can be revealed in samples with a fixed volume fraction of the magnetic particles, but with different particle sizes. This can be achieved by annealing samples with the same volume fraction to higher annealing temperature (T_A). Experimentally, one finds that $\rho_m \propto 1/r$. Because the interface area/volume in a granular system is $S \approx 3\ x_v/r$, as shown in Equation 4, where x_v is the volume fraction, evidently $\rho_m \propto S$. Thus GMR is due to spin-dependent scattering at the interfaces of the particles (67).

The dependence of ρ_m on x_v is shown in Figure 11, where $\rho(0)$, ρ_m, and

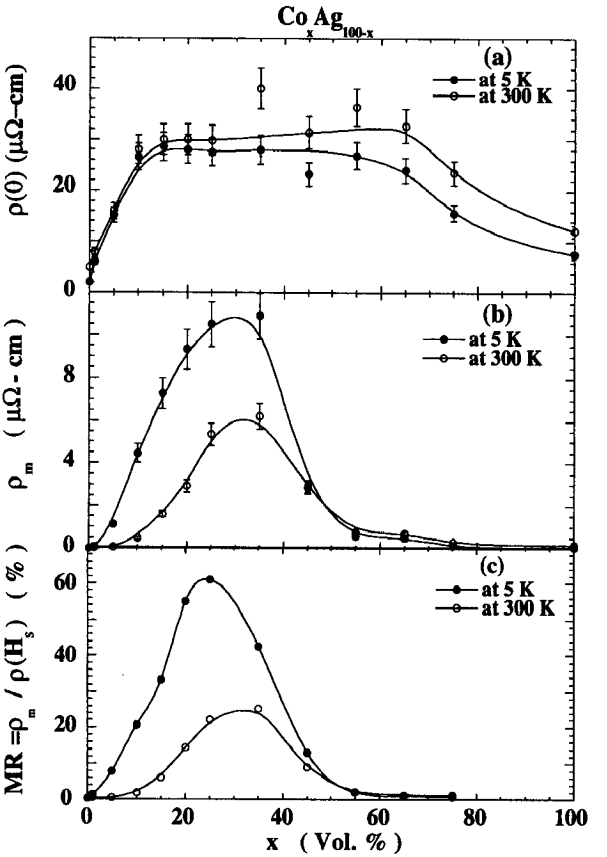

Figure 11 The values of (*a*) resistivity $\rho(0)$, (*b*) magnetic resistivity ρ_m, and (*c*) MR = $\rho_m/\rho(0)$ of Co-Ag as a function of Co content in vol %. The values at 5 and 300 K are denoted by solid and open circles, respectively.

GMR of Co-Ag with $0 \leqslant x_v \leqslant 1$ are shown (32). The value of $\rho(0)$ initially rises when Co is first introduced, reaches a plateau for a broad range of Co contents, and decreases towards the pure Co limit. The value of ρ_m increases from 0, reaching a maximum at about $x_v \approx 25\%$, before decreasing to very small value at $x_v \approx 55\%$, which is just the percolation threshold of a granular solid, beyond which a connecting network of Co is formed and there is no GMR. As shown in Equation 3, at $x_v \approx 25\%$, the spacing between particles is about the size of the particle.

We next compare GMR results of three systems of $Co_{20}Cu_{80}$, $Fe_{30}Ag_{70}$, and $Co_{20}Ag_{80}$ as a function of the annealing temperature (T_A), which, after phase separation, produces particles of larger sizes (76). As shown in Figure 12, in all cases, $\rho(0)$ and ρ_m decrease with increasing T_A. However, because the rates of decrease for $\rho(0)$ and ρ_m are different, the GMR may

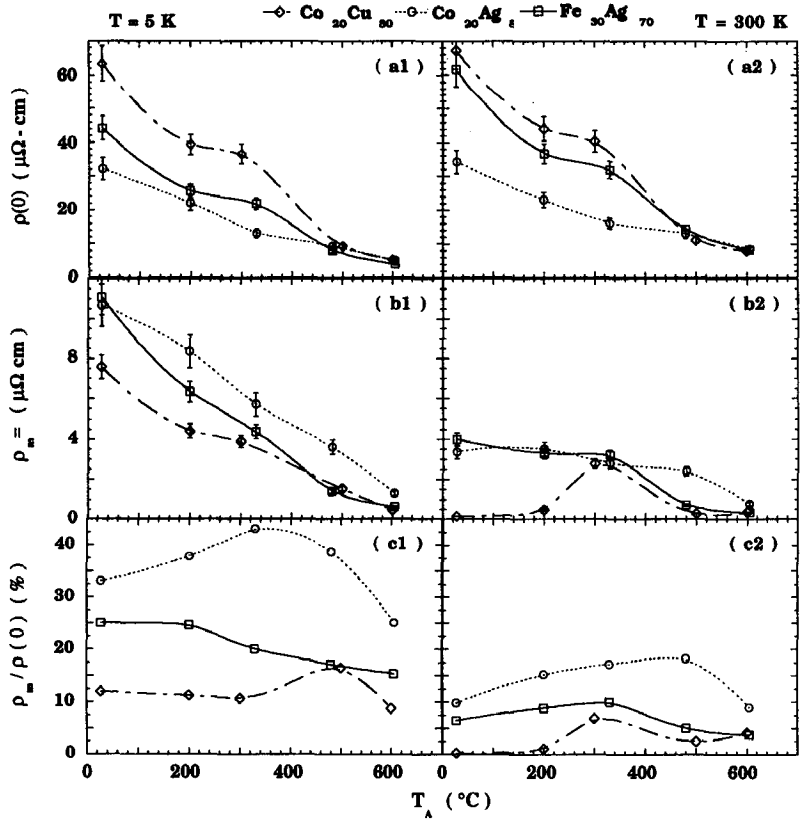

Figure 12 Resistivity [$\rho(0)$], magnetic resistivity (ρ_m) and MR = $\rho_m/\rho(0)$ at 5 and 300 K as a function of annealing temperature (T_A) of $Co_{20}Cu_{80}$, $Fe_{30}Ag_{70}$ and $Co_{20}Ag_{80}$.

be monotonically decreasing (e.g. $Fe_{30}Ag_{70}$ at 5 K), or showing a broad maximum (e.g. $Co_{20}Ag_{80}$ and $Co_{20}Cu_{80}$ at 5 K). It is interesting to note that for large ferromagnetic particles ($T_A = 600°C$), the differences among the three systems become small; in particular, the values $\rho(0)$ and ρ_m are quite similar. As shown in the lowest panel in Figure 12, among the three systems, the GMR effect is the largest in Co-Ag and smallest in Co-Cu. This is because $\rho(0)$ is the smallest and ρ_m the largest in Co-Ag, manifesting the fact that the effect size of GMR is the combination of both $\rho(0)$ and ρ_m.

Although the first observations of GMR in granular solids were made in Co-Cu alloys after phase separation of the metastable alloys by either post-annealing or deposition at elevated temperatures, these granular materials can also be achieved by other techniques. For example, Co-Cu, Fe-Ag, and Co-Ag alloys made by molecular beam epitaxy (MBE) at elevated substrate temperatures (74, 77, 78), and Co-Cu alloys made by melt-spinning technique (75), also have exhibited GMR. In the MBE-made, epitaxially grown granular films, small-angle x-ray diffraction measurements (77, 78) also implied interfacial spin-dependent scattering as the GMR mechanism, in agreement with the conclusion made earlier (67). It should be mentioned that some intended multilayers (e.g. Co/Ag, Co/Cu) may have granular-like entities at the interfaces, resulting in unexpectedly large MR effects. Hylton et al have in fact deliberately disrupted multilayers of permalloy/Ag to capture GMR with a small saturation field (79).

The main technological implications of GMR lie in magnetic field sensing. Of these, the most important are magnetoresistive heads for magnetic recording applications, motion and position sensors, and devices that currently use Hall-effect sensors. Many GMR materials already have sufficiently high sensitivity to displace Hall-effect devices. Magnetoresistive head application requires very small saturation fields, of the order of 10 Oe. The saturation fields for GMR materials have steadily been reduced to values of about 30 Oe (80, 81). The rapid advancement suggests that some or all of the applications mentioned may mature in the near future.

HALL RESISTIVITY (ρ_{xy})

The diagonal element of the magnetoresistivity tensor is the magnetoresistivity (ρ_{xx}), and the off-diagonal element is the Hall resistivity (ρ_{xy}). The Hall resistivitiy of magnetic metals can be expressed as (82)

$$\rho_{xy} = R_0 H + \rho_{xy}^M, \qquad 14.$$

where the first term is the ordinary Hall resistivity, which is linear in H, and the Hall constant $R_0 = 1/nec$ measures the carrier density (n). The second term in Equation 14 is the extraordinary Hall resistivity for magnetic metals

$$\rho_{xy}^{M} = R_s 4\pi M, \qquad 15.$$

which can be readily extracted by removing the linear R_0H part from ρ_{xy}.

The results of magnetoresistivity (ρ_{xx}), Hall resistivity (ρ_{xy}), extraordinary Hall resistivity (ρ_{xy}^{M}), and global magnetization (M) of granular $Co_{20}Ag_{80}$ ($T_A = 200°C$) are shown in Figure 13. An essential point concerning the extraordinary Hall resistivitiy of a granular solid, for that matter any magnetic material, is its field dependence. As is clearly illustrated in Figure 13, because the reproducible field-cycled results of ρ_{xy}^{M} and M have the same field dependence (i.e. the two hysteresis loops are essen-

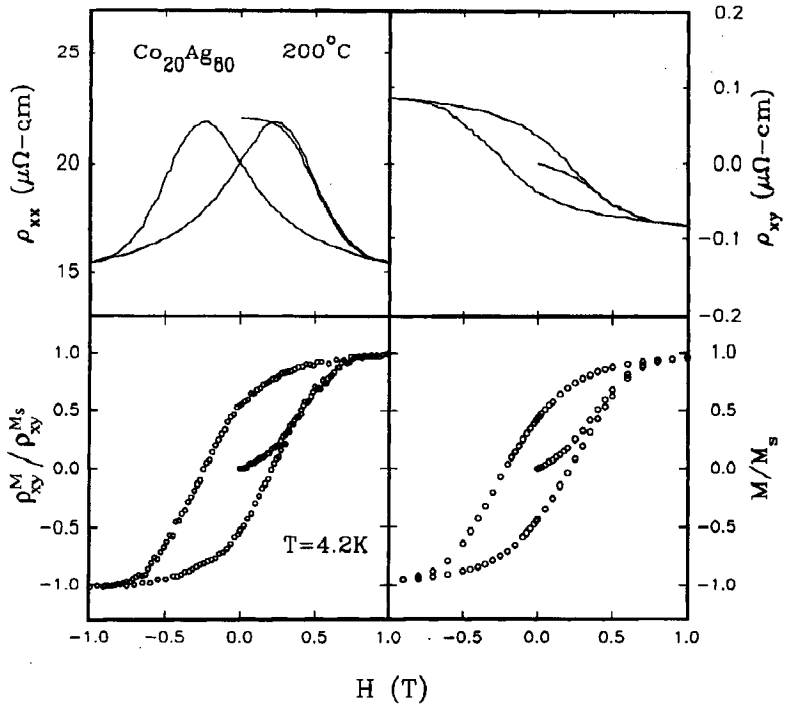

Figure 13 Magnetoresistivity (ρ_{xx}), Hall resistivity (ρ_{xy}), extraordinary Hall resistivity (ρ_{xy}^{M}) and global magnetization (M) of granular $Co_{20}Ag_{80}$ annealed at $T_A = 200°C$. In each case, the initial curve is not reproducible upon field cycling. The results of ρ_{xy}^{M} and M are plotted in reduced units to illustrate that the two hysteresis loops have the same shape. Hence the value of R_s in $\rho_{xy}^{M} = 4\pi R_s M$ is independent of field.

tially identical), ρ_{xy}^{M} and M are proportional to each other, therefore R_s is independent of field (67). It is important to emphasize again that because the initial curves are not reproducible, they cannot be used reliably to determine the correlation among various transport properties, and in particular, to determine the field dependence of R_s, or lack thereof.

In ordinary magnetic metals and alloys, the anisotropic MR is small, both R_s and ρ_{xx} are nearly independent of field. In these cases, the extraordinary Hall constant has been found to be related to the magnetoresistivity,

$$R_s = a\rho_{xx} \quad \text{(skew scattering)}, \qquad 16.$$

and

$$R_s = b(\rho_{xx})^2 \quad \text{(side-jump)}, \qquad 17.$$

according to the different scattering processes (82). There are attempts in the literature to use functions such as $R_s = a\rho_{xx} + b(\rho_{xx})^2$ to describe the extraordinary Hall resistivity of traditional magnetic alloys, multilayers, and granular solids (83), taking advantage of the additional freedom in fitting. However, because a and b are allowed to be of either sign and of any magnitude, the validity of such practices remains dubious. In granular solids, $\rho_{xx}(H)$ has a strong field dependence and R_s is essentially field-independent, thus R_s cannot be any actual function of $\rho_{xx}(H)$. In materials that exhibit GMR, as long as R_s is found to be independent of field, any exercises describing R_s as a function of $\rho_{xx}(H)$ would be futile. However, it has been found in granular Co-Ag that R_s scales with $(\rho_{xx})^{3.7}$ (67), using the values of either $\rho_{xx}(0)$ or $\rho_{xx}(8T)$. Such an unusual scaling is not well understood at present. Recently, very large finite-size effects in ρ_{xy}^{M} have also been observed in granular solids (84). These unusual characteristics of the extraordinary Hall resistivity are some of the outstanding issues in the magneto-transport properties of granular solids.

MAGNETO-THERMAL CONDUCTIVITY (κ)

Virtually all transport studies on multilayer and granular systems have been focused exclusively on electronic transport, one of several transport phenomena, all of which are essential for a complete understanding of the intriguing transport properties in these magnetically inhomogeneous systems. To date, very few studies have been made on thermal conductivity and thermoelectric power. The lack of thermal transport studies of thin films stems in part from experimental difficulties. Although resistivity measurements on thin-film samples can utilize any insulating substrate,

such samples are generally unsuitable for thermal transport measurements. Some of the major difficulties lie in the uncertainty in account for heat transfer through substrates much thicker than the films and the requirement of large specimens for thermometry.

Piraux et al reported the first thermal transport measurements on granular solids using large (cms), thick (about 100 μm), and substrate-free samples (85). The temperature dependence of the thermal conductivity (κ) of granular $Co_{20}Ag_{80}$ ($T_A = 605°C$) from 2 K to 300 K has been measured. The well known Wiedemann-Franz (WZ) law states that

$$\frac{\kappa\rho}{T} = L_0 = 2.45 \times 10^{-8}\, V^2/K^2, \qquad 18.$$

where κ is the thermal conductivity, ρ is the electrical resistivity, T the absolute temperature, and L_0 the Lorenz number. For ordinary metals, thermal conduction is purely electronic, and the WZ law is valid at low temperatures where the scattering is static. The WZ is also obeyed at high temperatures (above the Debye temperature), where the phonon energy becomes small compared with $k_B T$, and the dominating large-angle electron-phonon scattering events are quasi-static. In the intermediate temperature range (e.g. 40–250 K), the WZ law generally breaks down because of the importance of the small-angle electron-phonon scattering and inelastic scattering, and consequently, the values of $\kappa\rho/T$ are much smaller than L_0. These features are shown in Figure 14 by the solid curve. Most surprisingly, in granular Co-Ag, the WZ law is found to hold for the entire temperature range of 2–300 K. These results demonstrate the dominance of electronic thermal conductivity and large-angle scattering events throughout the temperature below the Debye temperature (85, 86).

Very large magneto-thermal conductivity has also been observed (85). For example, at 72 K, upon the application of a magnetic field, the thermal conductivity increases by 28%. The field dependence of the magneto-thermal conductivity is the same as that of the magnetoresistance. While the giant magnetoresistance is negative, the giant magneto-thermal conductivity is positive. Thus the magneto-thermal transport properties also satisfy the WZ law. These unusual thermal transport properties have not been observed in traditional metals and alloys.

CONCLUDING REMARKS

The unique features of granular solids are a collection of ultrafine metal particles with a narrow size distribution uniformly dispersed in an immiscible medium, which may be insulating or conducting, amorphous or

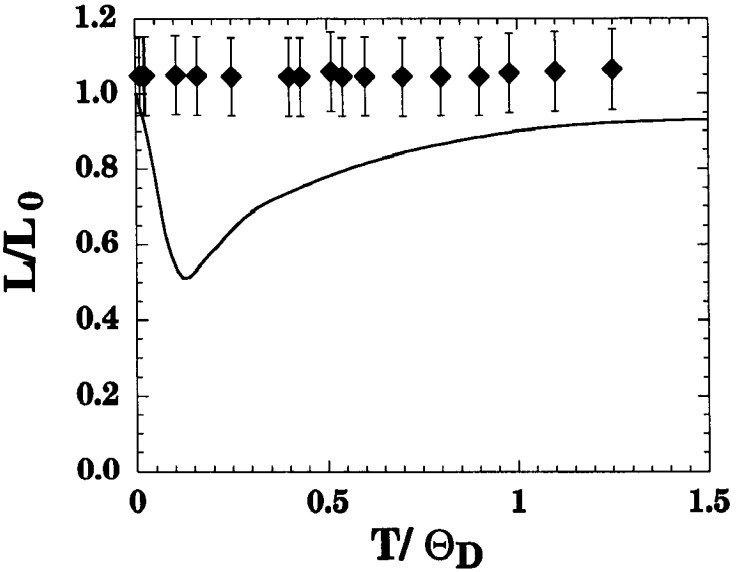

Figure 14 The values of L/L_0 of $Co_{20}Ag_{80}$, with $L = (\kappa\rho/T)$ and L_0 is the Lorenz number, as a function of temperature expressed in terms of the Debye temperature (Θ_D).

crystalline. By varying x_v and $2r$, one can greatly manipulate their physical properties, in general, and their magnetic and magneto-transport properties in particular. The enhanced magnetic and giant magneto-transport properties captured in granular solids cannot be realized in a bulk homogeneous solid. For granular magnetic solids with $x_v < x_p$, the single-domain magnetic properties and the associated superparamagnetism are amply displayed.

Granular magnetic solids also exhibit giant magneto-transport properties. The common feature of magnetic multilayers and magnetic granular solids that exhibit giant magneto-transport properties is that they are magnetically inhomogeneous with well-defined magnetic entities on the nanometer size. The importance of spin-dependent scattering events in giant magneto-transport properties appears to be well accepted (52, 87, 88). In order to quantitatively account for the rich and unconventional magneto-transport properties unveiled, theoretical endeavors should explicitly include these nanometer-size magnetic entities in the calculations. Considerable success has already been realized in magnetic multilayers (88). In the case of granular solids, the randomly dispersed ultrafine magnetic particles present special theoretical challenges. The most impressive advancement to date has been achieved by Maekawa and co-workers (89), who made calculations with the explicit inclusion of magnetic

particles. In the case of GMR, their theoretical results have already captured the MR dependence on $\langle \cos\theta \rangle^2$ and $1/r$, two key experimental results of GMR. Other magneto-thermal transport properties, particularly extraordinary Hall resistivity, magneto-thermal conductivity, and the Wiedemann-Franz law, await further theoretical and experimental exploration. One cannot emphasize enough the importance of measuring transport properties in absolute values. Otherwise, much of the discussion in the physics of the magneto-transport properties could not have proceeded.

Granular solids are indeed richly endowed. Even though extensive research began more than two decades ago, interesting new effects continue to be uncovered. As vividly made clear by the progress accumulated over these years, the exploration and the understanding of their unique properties require multi-disciplinary efforts, with theoretical and experimental expertise from fabrication, processing, characterization, measurements, and interpretations of various properties, as well as technological applications. If past experience is any indication, the fruitful study of granular solids may well extend into the next century.

ACKNOWLEDGEMENTS

This work is supported by Office of Naval Research Grant No. N00014-91-J-1633 and National Science Foundation Grant No. ECS92-02222. The author is indebted to colleagues who have contributed to the results mentioned in this paper: they include JQ Xiao, JS Jiang, JR Childress, A Gavrin, SH Liou, KM Unruh, A Tsoukatos, GC Hadjipanayis, G Xiao, P Xiong, JQ Wang, L Piraux and M Cassart.

Literature Cited

1. Falicov LM, Pierce DT, Bader SD, Gronsky R, Hathaway KB, et al. 1990. *J. Mater. Res.* 5: 1299–40
2. Dhez P, Weisbuch C. 1988. *Physics, Fabrication and Applications of Multilayered Structures*, New York: Plenum
3. Whitney TM, Jiang JS, Searson PC, Chien CL. 1993. *Science* 261: 1316–19
4. Abeles B. 1976. In *Applied Solid State Science: Advances in Materials and Device Research*, ed. R Wolfe, pp. 1–117. New York: Academic
5. Abeles B, Sheng P, Couts MD, Arie Y. 1975. *Adv. Phys.* 24: 407–61
6. Karch J, Birringer R, Gleiter H. 1987. *Nature* 330: 556–58
7. Siegel RW, Ramasamy S, Hahn H, Zongquan L, Ting L, Gronsky R. 1988. *J. Mater. Res.* 3: 1367–72
8. Hadjipanayis GC, Prinz GA. 1991. *Science and Technology of Nanostructured Magnetic Materials*, New York: Plenum
9. Kitada M. 1985. *J. Mater. Sci.* 20: 269–73
10. Childress JR, Chien CL, Nathan M. 1990. *Appl. Phys. Lett.* 56: 95–97
11. Childress JR, Chien CL. 1991. *J. Appl. Phys.* 70: 5885–87

12. Liou SH, Malhotra S, Shan ZS, Sellmyer DJ, Nafis S, et al. 1991. *J. Appl. Phys.* 70: 5882–84
13. Chien CL. 1991. *J. Appl. Phys.* 69: 5267–72
14. Sheng P. 1988. *Phys. Rev. Lett.* 45: 60–63
15. Matijevic E. 1989. *Mater. Res. Soc. Bull.* XIV: 18–20
16. Luborsky FE. 1961. *J. Appl. Phys.* 32: 171S–83S
17. Yiping J, Hadjipanayis GC, Sorenson CM, Klabunde KJ. 1989. *J. Magn. Magn. Mater.* 79: 321–26
18. Berkowitz AB, Walter JL, Wall KF. 1982. *Phys. Rev. Lett.* 49: 1484–87
19. Ambrose T, Gavrin A, Chien CL. 1992. *J. Magn. Magn. Mater.* 116: L311–14
20. Tasaki A, Tomiyana S, Iida S. 1965. *Jpn. J. Appl. Phys.* 4: 707–11
21. Shull RD, Ritter JJ. 1988. In *Physical Phenomena in Granular Materials*, ed. GD Cody, TH Geballe, P Sheng, pp. 435–40. Amsterdam: North Holland
22. Gavrin A, Chien CL. 1990. *J. Appl. Phys.* 67: 938–42
23. Liou SH, Chien CL. 1988. *J. Appl. Phys.* 63: 4240–42
24. Logothetis EM, Kaiser WJ, Plummer HK, Shinozak SS. 1986. *J. Appl. Phys.* 60: 2548–52
25. Tsoukatos A, Wan H, Hadjipanayis GC, Papaefthymiou V, Kostikas A, Simopoulos A. 1993. *J. Appl. Phys.* 73: 6967–69
26. Vossen JL, Kern W. 1991. *Thin Film Processes*, Vols. 1, 2. New York: Academic
27. Childress JR, Chien CL. 1991. *Phys. Rev. B* 43: 8089–93
28. Chien CL, Unruh KM. 1983. *Phys. Rev. B* 28: 1214–18
29. Xiao JQ, Jiang JS, Chien CL. 1992. *Phys. Rev. B* 46: 9266–69
30. Deleted in proof
31. Deleted in proof
32. Xiao JQ, Jiang JS, Chien CL. 1993. *Mater. Res. Soc. Proc. Nanophase and Nanocomposite Materials, No.* 286, ed. S Komarneni, JC Parker, GJ Thomas, pp. 197–207. Pittsburgh: Mater. Res. Soc.
33. Morrish AH. 1965. *Physical Principles of Magnetism*, New York: Wiley
34. Jacobs IS, Bean CP. 1963. In *Magnetism III*, ed. GT Rado, H Suhl, pp. 271–350. New York: Academic
35. Gittleman JL, Goldstein Y, Bozowski S. 1972. *Phys. Rev. B* 5: 3609–20
36. Xiao G, Liou SH, Levy A, Taylor JN, Chien CL. 1986. *Phys. Rev. B* 34: 7573–77
37. Kittel C, Galt JK. 1946. *Phys. Rev. B* 70: 965–71
38. Stoner EC, Wohlfarth EP. 1948. *Philos. Trans. R. Soc. London Ser. A* 240: 599–642
39. Kittel C. 1949. *Rev. Mod. Phys.* 21: 541–83
40. Xiao G, Chien CL. 1987. *Appl. Phys. Lett.* 51: 1280–82
41. Liou SH, Chien CL. 1988. *Appl. Phys. Lett.* 52: 512–14
42. Paparazzo E, Dormann JL, Fiorani D. 1983. *Phys. Rev. B* 28: 1154–57
43. Shah SI, Unruh KM. 1991. *Appl. Phys. Lett.* 59: 3485–87
44. Xiao JQ, Jiang JS, Chien CL. 1992. *Phys. Rev. Lett.* 68: 3749–52
45. Kneller EF, Luborsky FE. 1963. *J. Appl. Phys.* 34: 656–58
46. Dormann JL, Fiorani D, Tholence JL, Sell C. 1983. *J. Magn. Magn. Mater.* 35: 117–20
47. Morop S, Topsoe T, Clausen BC. 1982. *Phys. Scr.* 25: 713–19
48. Childress JR, Chien CL, Rhyne JJ, Erwin RW. 1992. *J. Magn. Magn. Mater.* 104–107: 1585–86
49. Xiao G, Chien CL. 1987. *J. Appl. Phys.* 61: 3308–10
50. Chantrell RW, Wohlfarth EP. 1983. *J. Magn. Magn. Mater.* 40: 1–11
51. Bennett LH, McMichael RD, Swartzendruber LJ, Shull RD, Watson RE. 1992. *J. Magn. Magn. Mater.* 104–105: 1094–97
52. Baibich MN, Broto JM, Fert A, Nguyen van Dau F, Petroff F, et al. 1988. *Phys. Rev. Lett.* 61: 2472–75
53. Binasch G, Grünberg P, Saurenbach P, Zinn W. 1989. *Phys. Rev. B* 39: 4828–30
54. Parkin SSP, Bhadra R, Roche KP. 1991. *Phys. Rev. Lett.* 66: 2152–55
55. Pratt WP Jr, Lee SF, Slaughter JM, Loloee R, Schroeder PA, Bass J. 1991. *Phys. Rev. Lett.* 66: 3060–63
56. Chaiken A, Prinz GA, Krebs JJ. 1990. *J. Appl. Phys.* 87: 4892–94
57. Dieny B, Speriosu VS, Parkin SSP, Gurney BA, Wilhoit DR, Mauri D. 1991. *Phys. Rev. B* 43: 1297–1300
58. Johnson MT, Purcell ST, McGee MWE, Coehoorn R, van de Stegge J, Hoving W. 1992. *Phys. Rev. Lett.* 68: 2688–91
59. Shinjo T, Yamamoto H. 1990. *J. Phys. Soc.* 59: 3061–64
60. Chen Y, Florczak JM, Dahlberg ED. 1992. *J. Magn. Magn. Mater.* 104–105: 1907–8
61. Fullerton EE, Kelly DM, Guimpel J, Schuller IK, Bruynseraede Y. 1992. *Phys. Rev. Lett.* 68: 859–62
62. Tsui F, Chen B, Barlett D, Clarke R, Uher C. 1994. *Phys. Rev. Lett.* 72: 740–43
63. Rossiter PL. 1987. *The Electrical Resis-*

tivity of Metals and Alloys, Cambridge: Cambridge Univ. Press
64. McGuire TR, Potter RI. 1975. *IEEE Trans. Magn.* MAG-11: 1018–38
65. Berkowitz A, Young AP, Mitchell JR, Zhang S, Carey MJ, et al. 1992. *Phys. Rev. Lett.* 68: 3745–48
66. Barnard JA, Watnis A, Tan M, Haftek E, Parker MR, Watson ML. 1992. *J. Magn. Magn. Mater.* 114: L230–34
67. Xiong P, Xiao G, Wang JQ, Xiao JQ, Jiang JS, Chien CL. 1992. *Phys. Rev. Lett.* 69: 3220–23
68. Jiang JS, Xiao JQ, Chien CL. 1992. *Appl. Phys. Lett.* 61: 2362–64
69. Chien CL, Xiao JQ, Jiang JS. 1993. *J. Appl. Phys.* 73: 5309–14
70. Carey MJ, Young AP, Starr A, Rao D, Berkowitz AE. 1992. *Appl. Phys. Lett.* 61: 2935–37
71. Tsoukatos A, Wan H, Hadjipanayis GC. 1992. *Appl. Phys. Lett.* 61: 3059–61
72. Xiao G, Wang JQ, Xiong P. 1993. *Appl. Phys. Lett.* 62: 42–44
73. Wang JQ, Xiong P, Xiao G. 1993. *Phys. Rev.* B47: 8341–44
74. Parkin SSP, Farrow RFC, Rabedeau TA, Marks RF, Harp GR, et al. 1993. *Europhys. Lett.* 22: 455–62
75. Dieny B, Chamberod A, Genin JB, Rodmacq B, Teixeira SR, et al. 1993. *J. Magn. Magn. Mater.* 126: 433–36
76. Xiao JQ, Jiang JS, Chien CL. 1993. *IEEE Trans. Magn.* MAG-29: 2688–93
77. Rabedeau TA, Toney MF, Marks RF, Parkin SSP, Farrow RFC, Harp GP. 1993. *Phys. Rev. B* 48: 16810–13
78. Thangaraj N, Echer C, Krishnan KM, Farrow RFC, Marks RF, Parkin SSP. 1994. *J. Appl. Phys.* 75: 6900–2
79. Hylton TL, Coffey KR, Parker MA, Howard JK. 1993. *Science* 261: 1021–24
80. Parkin SSP, Farrow RFC, Marks RF, Cebollada, Harp GR, Savoy RJ. 1994. *Phys. Rev. Lett.* 72: 3718–22
81. Hossain S, Seale D, Qiu G, Barnard JA, Fujiwara H, Parker MR. 1994. *J. Appl. Phys.* 75: 7067–69
82. Berger L, Bergmann G. 1979. In *The Hall Effect and Its Applications*, ed. CL Chien, CR Westgate, pp. 55–76. New York: Plenum
83. Sato H, Kumano T, Aoki Y, Kaneko T, Yamamoto R. 1993. *J. Phys. Soc. Jpn.* 62: 416
84. Wang JQ, Xiao G. 1995. *Phys. Rev. B.* 51:
85. Piraux L, Cassart M, Jiang JS, Xiao JQ, Chien CL. 1993. *Phys. Rev. B* 48: 638–41
86. Piraux L, Cassart M, Bayot V, Jiang JS, Xiao JQ, Chien CL. 1993. *IEEE Trans. Magn.* MAG-29: 2700–4
87. Camley RE, Barnas J. 1989. *Phys. Rev. Lett.* 63: 664–67
88. Valet T, Fert A. 1993. *J. Magn. Magn. Mater.* 121: 378–82
89. Asano Y, Oguri A, Inoue J, Maekawa S. 1994. *Phys. Rev. B* 49: 12,831–34

Annual Review of Materials Science
Volume 25, 1995

CONTENTS

▷ Keynote Topic: Electronic Materials